

Self-consistent modeling of magnetic fields and plasmas in the inner magnetosphere: Application to a geomagnetic storm

Sorin Zaharia,¹ V. K. Jordanova,^{2,3} M. F. Thomsen,¹ and G. D. Reeves¹

Received 16 January 2006; revised 29 May 2006; accepted 29 June 2006; published 5 October 2006.

[1] A geomagnetic storm model needs to take into account the coupling between magnetic field and plasma, as the storm-time field in the inner nightside magnetosphere can be very depressed compared to that of the Earth dipole, thus significantly modifying plasma transport. In this paper we extend our previous “one-way” coupling between a kinetic ring current model and a magnetospheric force-balance model to a fully magnetically self-consistent approach, in which the force-balanced fields are fed back into the kinetic model to guide its evolution. The approach is applied to simulating the 21–23 April 2001 “GEM Storm Challenge” event. We use boundary and initial conditions for the kinetic model from several spacecraft, and magnetic flux boundaries for the equilibrium code from an empirical magnetic field model. We find significant differences in the self-consistent results compared to those obtained from the kinetic model with a dipolar background field (with the same particle boundary conditions and electric fields), due mainly to changes in the particle drifts. In addition to large depressions in the nightside magnetic field values compared to a dipolar field, we also find significantly lower particle density and perpendicular plasma pressure in the inner magnetosphere in the self-consistent case, as well as local, narrow pressure peaks and strongly enhanced plasma β_p in localized regions on the nightside.

Citation: Zaharia, S., V. K. Jordanova, M. F. Thomsen, and G. D. Reeves (2006), Self-consistent modeling of magnetic fields and plasmas in the inner magnetosphere: Application to a geomagnetic storm, *J. Geophys. Res.*, *111*, A11S14, doi:10.1029/2006JA011619.

1. Introduction

[2] Models of the inner magnetosphere, crucial in the study of geomagnetic storms, need to take into account the physical coupling between plasma and fields. In particular, the coupling between plasma and magnetic field is very important: a realistic magnetic field is needed, for example, for the correct modeling of particle drifts, as drift-shell splitting [Roederer, 1967] appearing in nondipolar fields leads to changes in the particle drifts and pitch angle distribution. Many physical models of the inner magnetosphere have so far mainly used the dipole approximation for the magnetic field; however, both observations and computational studies report large depressions in the field during the main phase of storms [e.g., Cahill, 1973; Tsyganenko *et al.*, 2003; Zaharia *et al.*, 2005]. Such studies show that the fields induced by magnetospheric current systems become important even close to Earth during storms; therefore using

the dipolar approximation even at $L \sim 3$ –4 to model such events can be problematic [Tsyganenko *et al.*, 2003]. It is thus clear that more realistic magnetic fields need to be used for storm modeling, and the plasma and the magnetic field should represent a self-consistent configuration obeying the plasma momentum equation.

[3] The self-consistent coupling between magnetic fields and plasmas in the inner magnetosphere has so far not been well modeled and understood. There have been however several efforts toward that eventual goal, some of which will be very briefly discussed below.

[4] Quite popular in the magnetospheric community is the use of empirical models [e.g., Tsyganenko, 1989; Tsyganenko and Stern, 1996; Tsyganenko and Sitnov, 2005] that specify the magnetic field only. Their drawback is that they do not incorporate any plasma information: the fields of the empirical models are not built to be in force balance with plasma pressure [Zaharia and Cheng, 2003b]; i.e., they are not self-consistent. Some ad hoc methods have been developed for improving an empirical specification (but not necessarily making the field fully consistent with the pressure), including either choosing the best existing model for a particular situation [Chen *et al.*, 2005], or modifying the parameters of an empirical one to suit a particular event [Ganushkina *et al.*, 2002]. An alternative to using an empirical field is employing global magnetohydro-

¹Space Science and Applications, Los Alamos National Laboratory, Los Alamos, New Mexico, USA.

²Space Science Center, University of New Hampshire, Durham, New Hampshire, USA.

³Now at Space Science and Applications, Los Alamos National Laboratory, Los Alamos, New Mexico, USA.

dynamics (MHD) models [e.g., *Raeder et al.*, 1995]. While time dependent, the MHD fields are not consistent with particle populations computed by more realistic kinetic models: for one, plasma is anisotropic in the inner magnetosphere while the MHD models assume isotropy; probably even more importantly, the single-fluid MHD treatment does not include the gradient and curvature drifts (the dominant motion of the pressure-bearing inner magnetosphere particles) and thus cannot provide an adequate description of the inner magnetosphere [e.g., *De Zeeuw et al.*, 2004].

[5] A physically more realistic model in the inner magnetosphere is RCM [*Harel et al.*, 1981] an isotropic convection model that, unlike MHD, includes all relevant particle drift physics, and which has been using nondipolar fields for a while [*Fok and Moore*, 1997; *Sazykin et al.*, 2002]. RCM has been coupled with a magnetofriction code [*Hesse and Birn*, 1993; *Toffoletto et al.*, 1996, 2001; *Lemon et al.*, 2004], and in that approach the plasma (considered isotropic) and the field are self-consistent. On a parallel track, RCM has also been coupled with global MHD models [*Toffoletto et al.*, 2004; *De Zeeuw et al.*, 2004]. While the coupled models are vast improvements over MHD alone in the inner magnetosphere, they still rely on MHD to advance the fields, and they also treat plasma isotropically. Plasma is however anisotropic in the inner magnetosphere, and the anisotropy leads to the growth of waves such as electromagnetic ion cyclotron (EMIC) waves that are crucial in various acceleration and loss processes that affect the particles. Finally, we briefly note that another line of research in the community is seeking to model the interaction between plasma and electric, rather than magnetic, fields self-consistently [e.g., *Ridley and Liemohn*, 2002; *Khazanov et al.*, 2003; *Ebihara et al.*, 2004; *Liemohn et al.*, 2005].

[6] The modeling approach presented in this paper is a fully anisotropic magnetically self-consistent formulation that completely relegates the task of describing plasma transport to the kinetic RAM code [*Jordanova et al.*, 1997]. We use the plasma pressure distributions from RAM to calculate the global three-dimensional (3-D) magnetic field in force balance with them, and finally we feed that field back into the RAM code to drive its evolution. The approach is thus a full (“two-way”) coupling between RAM and the 3-D equilibrium code. An initial “one-way coupling” was developed by *Zaharia et al.* [2005] and applied to a magnetic storm simulation. In that study, the RAM code was used to follow the particles in the Earth dipole field, and then the magnetic field in force balance with the particle pressure was obtained; however, the field was not fed back into RAM. The one-way coupling nevertheless showed that the magnetic field values that equilibrate realistic pressures during the main phase of a storm are very depressed compared to the Earth dipole field, and that plasma pressure has a very strong effect on the field due to the high plasma β_p . In view of those results, *Zaharia et al.* [2005] pointed out that a magnetically self-consistent approach (i.e., a two-way coupling) was a clearly needed feature in geomagnetic storm modeling.

[7] The present work is such a two-way coupling, whereby particle motion affects the magnetic field and the field affects the particles in return. One assumption of our approach is that “quasi-static” magnetospheric equilibria

exist at all times [*Wolf*, 1983], except for periods of explosive activity (i.e., substorm expansion phases). Such equilibria characterize not only quiet times, but also driven events such as storms, if one is only interested in the regions on closed field lines away from the magnetopause, and in the absence of dipolarizations or compressions of the whole magnetosphere by sudden solar wind impulses (dynamic pressure changes). In the inner magnetosphere plasma flows are slow compared to the fast mode speed [*Wolf*, 1983] at most times, and the quasi-static approximation is valid there. In particular, for the event simulated in this study, geosynchronous LANL observations show no magnetopause crossings and no significant dipolarizations. Furthermore, even though substorms can and do occur during the main phase of some storms, their overall effects are found to be relatively small [*Chen et al.*, 1994] over the cycle of substorm field stretching and dipolarization.

[8] With the slow-flow assumption, we use our 3-D equilibrium code, extended to anisotropic pressure [*Zaharia et al.*, 2004], to compute force-balanced magnetic fields and plasmas, with magnetic flux boundaries from empirical models and anisotropic plasma pressures in the equatorial plane from RAM. The RAM code [*Jordanova et al.*, 1997] has been used thus far to compute the bounce-averaged motion in a dipolar field, with various loss mechanisms taken into account: charge exchange, Coulomb scattering, and wave-particle interactions. Recent developments [*Jordanova and Miyoshi*, 2005] have added radial diffusion and relativistically treated electrons. To be used in this study, the RAM formalism has been updated to include arbitrary magnetic fields. The RAM model uses boundary conditions at geosynchronous orbit based on observations. A description of the RAM formalism with arbitrary magnetic fields, as well as extensive comparisons of RAM results with observations, can be found in a companion paper [*Jordanova et al.*, 2006].

[9] Our equilibrium approach is unique in its ability to compute 3-D magnetic fields in force balance with prescribed anisotropic pressures; this feature is important for storm studies, as the inner magnetospheric plasma is often anisotropic, typically with $P_{\perp} > P_{\parallel}$. Furthermore, unlike other model coupling studies, our technique does not change the pressures in the course of computing the field, instead relegating the plasma transport description to the kinetic RAM model.

2. Models

2.1. Equilibrium Model With Anisotropic Pressure

[10] We use a computational approach in flux coordinates (Euler potentials) which is a direct extension [*Zaharia*, 2003; *Zaharia et al.*, 2004] of the isotropic pressure case [*Cheng*, 1995; *Zaharia and Cheng*, 2003a]. The code solves the 3-D force-balance equation:

$$\mathbf{J} \times \mathbf{B} = \nabla \cdot \mathbf{P} \quad (1)$$

where \mathbf{P} is the general pressure tensor. With anisotropic pressure, denoting by P_{\perp} and P_{\parallel} the pressures perpendicular and parallel to the field, respectively, we have

$$\nabla \cdot \mathbf{P} = \nabla P_{\perp} - \nabla \cdot [(P_{\perp} - P_{\parallel})\mathbf{bb}]$$

and equation (1) becomes

$$\sigma \mathbf{J} \times \mathbf{B} = \nabla P_{\perp} - (\mathbf{B} \cdot \nabla \sigma) \mathbf{B} + (1 - \sigma) \nabla \left(\frac{B^2}{2} \right) \quad (2)$$

with $\sigma = 1 + (P_{\perp} - P_{\parallel})/B^2$.

[11] One can express the magnetic field vector in terms of Euler potentials as $\mathbf{B} = \nabla \alpha \times \nabla \beta$ (we use this notation here, which is different from the (ψ, α) notation elsewhere, including in the work of *Zaharia et al.* [2005], for consistency with common nomenclature in the space physics community). In this representation the magnetic field lines are given by the intersection of the constant α and β surfaces. Then, equation (2) can be decomposed into two “quasi-2-D” inhomogeneous elliptic partial differential equations for the Euler potentials α and β :

$$\nabla \cdot \left[(\nabla \alpha)^2 \nabla \beta - (\nabla \alpha \cdot \nabla \beta) \nabla \alpha \right] = - \frac{(\mathbf{B} \times \nabla \alpha)}{\sigma B^2} \cdot \left[\nabla P_{\perp} + (1 - \sigma) \nabla \left(\frac{B^2}{2} \right) \right] \quad (3)$$

$$\nabla \cdot \left[(\nabla \alpha \cdot \nabla \beta) \nabla \beta - (\nabla \beta)^2 \nabla \alpha \right] = - \frac{(\mathbf{B} \times \nabla \beta)}{\sigma B^2} \cdot \left[\nabla P_{\perp} + (1 - \sigma) \nabla \left(\frac{B^2}{2} \right) \right]. \quad (4)$$

[12] The equations above (which are expressed in the rationalized EMU system) are coupled quasi-2-D elliptic equations for each Euler potential, on surfaces on which the reciprocal potential is constant. They are solved together with two Maxwell's equations:

$$\nabla \times \mathbf{B} = \mu_0 \mathbf{J} \quad (5)$$

$$\nabla \cdot \mathbf{B} = 0 \quad (6)$$

[13] The system of equations (3)–(6) is not solvable analytically in general. We seek a numerical solution, using a Picard iteration procedure (keeping the nonlinear terms on the right-hand sides of equations (3) and (4) constant at each iteration). Our solution is sought in inverse form, i.e., rather than obtaining the \mathbf{B} components explicitly, we seek X , Y , and Z as functions of α , β , and χ (where χ is a coordinate along the field lines).

[14] What is needed for a unique 3-D solution then are the pressures P_{\perp} and P_{\parallel} at one point on each field line (in this study they are taken in the equatorial plane while magnetic moment and energy conservation provide their mapping along the field lines), as well as boundary conditions for the magnetic flux α (usually obtained from empirical field models [*Zaharia et al.*, 2004]). The condition for β is simply periodicity in the azimuthal direction, while the boundary conditions in the χ coordinate are obtained from our knowledge of the field and its Euler potentials at the ends of the field line (i.e., on the Earth's surface). In this study the field on the Earth's surface is taken to be dipolar, but further refinements such as using an IGRF field could be considered in the future.

[15] We note that realistic pressure is needed as input to the model, as the high plasma β_p (the ratio of plasma to magnetic pressure, not to be confused with the Euler potential β) is large near the equatorial plane; thus small plasma pressure variations can lead to significant changes in the field configuration. Furthermore, a stable equilibrium does not exist for all values of the anisotropy P_{\perp}/P_{\parallel} , as it will be destroyed by either a fire hose (for $P_{\perp}/P_{\parallel} < 1$) or a mirror or ion cyclotron instability (for large-enough $P_{\perp}/P_{\parallel} > 1$ [e.g., *Gary et al.*, 1997]).

[16] Our approach, owing to the inverse representation, also requires that the magnetic flux surfaces be nested, i.e., does not allow regions that include X or O-points; however, this is not a concern in the inner magnetosphere.

[17] Besides the values of α on the inner and outer magnetic flux surfaces, the shapes of those surfaces are needed as well. Both value and shape are obtained by field-line tracing of empirical magnetic field models [*Zaharia et al.*, 2004]. Those models are parameterized according to solar wind activity and other indices, thus reflecting the overall disturbance level in the magnetosphere. The computed 3-D magnetic field is, however, different everywhere from the empirical one, which is taken as an initial guess only. Even on the inner and outer magnetic flux boundaries (which are kept fixed), the magnetic field lines will slide to accommodate the input pressure gradients.

2.2. Kinetic RAM Model

[18] The kinetic ring current-atmosphere interactions model (RAM) [*Jordanova et al.*, 1994, 1997, 2001] numerically solves the relativistic evolution equation for the bounce-averaged particle distribution function [*Roederer*, 1970] in conservative form:

$$\begin{aligned} \left\langle \frac{dQ_l}{dt} \right\rangle &= \frac{\partial Q_l}{\partial t} + \frac{1}{R_0^2} \frac{\partial}{\partial R_0} \left(R_0^2 \left\langle \frac{dR_0}{dt} \right\rangle Q_l \right) + \frac{\partial}{\partial \phi} \left(\left\langle \frac{d\phi}{dt} \right\rangle Q_l \right) \\ &+ \frac{1}{\sqrt{E}} \frac{\partial}{\partial E} \left(\sqrt{E} \left\langle \frac{dE}{dt} \right\rangle Q_l \right) + \frac{1}{h(\mu)\mu} \frac{\partial}{\partial \mu} \\ &\left(h(\mu)\mu \left\langle \frac{d\mu}{dt} \right\rangle Q_l \right) = \left\langle \frac{dQ_l}{dt} \right\rangle_{\text{losses}} \end{aligned} \quad (7)$$

with $Q_l(R_0, \phi, \mu, t)$ the distribution function for species l , $dV = 8\pi\sqrt{2}m_l^3 R_0^2 \sqrt{E} \mu h(\mu) dR_0 d\phi dE d\mu$ the differential phase space volume, R_0 the equatorial plane radial distance, ϕ the azimuthal angle, E the particle kinetic energy, $\mu = \cos(\alpha_0)$ (α_0 is the equatorial pitch angle, not to be confused with the Euler potential α) and

$$h(\mu) = \frac{1}{2R_0} \int_{s_m}^{s'_m} \frac{ds}{\sqrt{1 - B(s)/B_m}} \quad (8)$$

which is proportional to the bounce period, being the so-called “half-bounce path length” [e.g., *Roederer*, 1970], normalized by $1/2R_0$. The brackets $\langle \rangle$ denote bounce-averaging. The RAM formalism is useful for tracking particles in regions where the first two invariants are conserved (i.e., changes in Q_l are negligible on the timescales of the gyro and bounce periods), which is the case at radial distances closer than $10 R_E$ from Earth.

[19] Equation (7) is solved in a circular domain in the equatorial plane defined by $2 R_E \leq R_0 \leq 6.5 R_E$ and

covering all local times. The kinetic energies of the particles considered are from 100 eV to 800 keV. The initial conditions are from POLAR, CLUSTER and AP8 [Jordanova and Miyoshi, 2005], while the boundary conditions are based on LANL/MPA [McComas et al., 1993] and SOPA measurements [Belian et al., 1992].

[20] Owing to the bounce-averaging, the evolution equation (7) is in four coordinates only: R_0 , ϕ , E , and μ . The RAM model includes various loss processes: charge exchange, Coulomb collisions, wave-particle interactions, as well as losses to the atmosphere. While recent developments [Jordanova and Miyoshi, 2005] also treat relativistic electrons and include a radial diffusion term on the right-hand side of equation (7), those features were not included in this study. As mentioned, the RAM code has so far used a dipolar magnetic field. For more details about RAM, including changes needed for this study to accommodate nondipole \mathbf{B} -fields, we refer the reader to our companion paper [Jordanova et al., 2006].

2.3. Computational Coupling Details

[21] In order to couple RAM with the equilibrium model, we use an iterative approach, whereby at each iteration RAM and the 3-D equilibrium code are run for the whole simulation time span. We compute the force-balanced field at each hour with pressures from RAM, after which we feed the field back into RAM. This process is repeated until approaching convergence. We use a large number of grid points in the equilibrium code, typically $N_\chi \times N_\alpha \times N_\beta = 101 \times 71 \times 141$, in order to resolve the high- β_p equilibria and accurately compute the integrals along the field lines described below. The resolution is sometimes further increased to allow the code to converge with the sharp pressure gradients that appear during the storm main phase. Typically, less than 7 iterations (i.e. 3-D code iterations for computing equilibria, not to be confused with iterations of the coupling process) are needed for convergence. When needed, a “blending” technique [Zaharia et al., 2004] is also used, through which a fraction of the solution of a previous 3-D code iteration is blended into the latest iterative 3-D solution; this improves numerical stability but increases the number of 3-D code iterations (we typically need in such cases 20 iterations with a blending parameter of 0.3 to achieve a reasonably good equilibrium).

2.3.1. Field-Line Integrals

[22] One side of the coupling, whereby the 3-D model uses pressure input from RAM, was discussed before [Zaharia et al., 2005]. We address here the second aspect, i.e., how RAM uses the magnetic field from the 3-D model. One simplifying factor is that the RAM model does not need the explicit 3-D field components, as for bounce-averaged quantities the magnetic field enters the RAM formulation through the purely field-geometric integrals $h(\mu)$ (defined in equation (8)) and

$$I(\mu) = \frac{1}{R_0} \int_{s_m}^{s'_m} \sqrt{1 - B(s)/B_m} ds, \quad (9)$$

where s_m and s'_m are the southern and northern mirror point coordinates, respectively, of a bouncing particle. While $h(\mu)$ has already been introduced as the normalized half-path

bounce length, $I(\mu)$ is related to the second adiabatic invariant J through $J = 2pR_0I(\mu)$ [Ejiri, 1978], where p is the particle momentum in the equatorial plane. The above integrals are easily solved in the equilibrium code coordinate system, as they are just 1-D integrals (over χ , the coordinate that parameterizes the distance along the field line). Indeed, with an equal arc length χ choice (i.e., equal $\Delta\chi$ corresponds to equal Δs), the field line distance is $s = \chi s_0/\pi$; therefore

$$\int_{s_m}^{s'_m} f(s) ds = \frac{s_0}{\pi} \int_{\chi_m}^{\chi'_m} f(\chi) d\chi,$$

where χ_m , the location of the mirror point, is determined from $B(\chi)$ by 1-D cubic spline interpolation.

[23] We use the QUADPACK adaptive integration routines DQAG and DQAGI [Piessens et al., 1983] to calculate the integrals for each (α, β) pair in the 3-D code. Finally, we need to project the computed quantities onto the RAM cylindrical coordinate system, i.e., from $h(\alpha, \beta; \mu)$ and $I(\alpha, \beta; \mu)$ to $h(R_0, \phi; \mu)$ and $I(R_0, \phi; \mu)$. We do this by a “gridding” technique that consists in a Delaunay triangulation (using the Qhull package [Barber et al., 1996]), followed by linear interpolation inside the triangle containing the point of interest $\{R_0, \phi\}$. We use nearest-neighbor interpolation to obtain quantities in the limited “buffer” regions (mostly on dayside) outside the 3-D code computational domain, but inside $6.5 R_E$ (due to the dayside flux surface compression).

[24] The field-line integrals are computed at each hour, and linear interpolation is used in RAM to obtain values in between. The two steps (integration and 2-D interpolation) are relatively fast and add little computational overhead to the equilibrium calculation, highlighting one advantage of an Euler potential coordinate approach for computational inner magnetosphere modeling.

2.3.2. Field-Line Integrals: Benchmarking

[25] Before employing the technique to modeling a geomagnetic storm we verified our calculation of h and I by comparing the numerical results obtained for a dipole field with analytical solutions. For a dipole, h and I depend on pitch angle only, not on the equatorial location of the field foot point, and very accurate (within 0.1%) approximate analytical values exist [Ejiri, 1978]. The results obtained for a dipole using our numerical method were found to be very close (most within 0.2%) to the values of [Ejiri, 1978] for all locations and pitch angles.

3. 3-D Code Inputs

3.1. Anisotropic Pressure

[26] The pressure input in the 3-D model consists of perpendicular/parallel pressures in the equatorial plane, obtained from moments of the RAM distribution function:

$$P_\perp = \int \frac{1}{2} m v^2 F \sin^2 \alpha_0 d\mathbf{p}$$

$$P_\parallel = \int m v^2 F \cos^2 \alpha_0 d\mathbf{p}$$

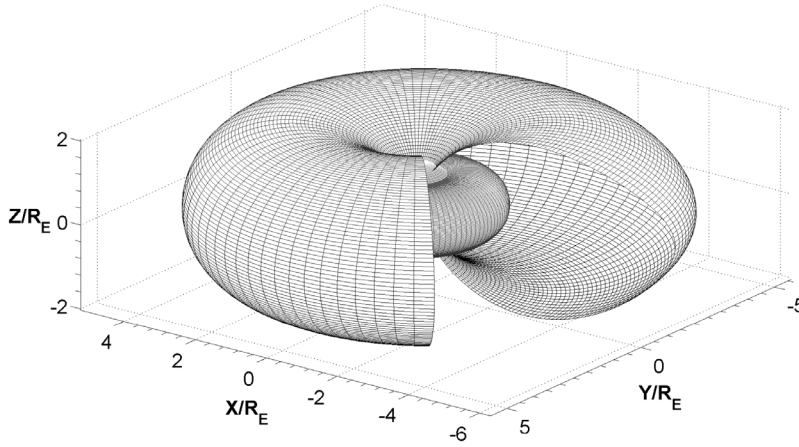


Figure 1. One computational domain for performing the three-dimensional equilibrium calculations, obtained by tracing magnetic field lines from the T89 model with $K_p = 6$.

[27] The pressure maps from RAM are generally too rough for being used directly in the 3-D code, as very smooth functions are needed in the 3-D model to ensure convergence. To this end, we use spline interpolation to transform the pressure map in the equatorial plane into a smoother function. We stress here that the RAM pressure profiles are kept spatially fixed in the equatorial plane, and therefore the functionals $P_{\perp}(\alpha, \beta)$ and $P_{\parallel}(\alpha, \beta)$ do change at each equilibrium code iteration in the flux coordinate space until equilibrium is achieved.

[28] The pressures given by the RAM model are from three ion species (H^+ , He^+ , and O^+). We neglect the electron pressure contribution as it is (in the RAM output) small ($\sim 2\%$) during quiet times and only reaches maximum values of $\sim 10\%$ near Dst minima [Jordanova and Miyoshi, 2005]. While an isotropic pressure can simply be mapped along \mathbf{B} -field lines as it is constant along the field line in equilibrium, this is not so for the anisotropic case. However, we use the fact that the distribution changes slowly enough so that we can employ energy and magnetic moment conservation (basically apply Liouville's theorem) to obtain the anisotropic pressure values along the magnetic field lines. While in our previous work we neglected the existence of the loss cone in this collisionless mapping, here we improve the treatment by considering the empty loss cone formulation described by equation (8) of Liemohn [2003]:

$$P_{\parallel} = P_{\parallel r}^* \frac{1 + A^*}{1 + A^* R_B} \left[\frac{R_{BI} - 1}{R_{BI} - R_B} \right]^{1/2} \left(1 - \frac{1 + A^* R_B}{R_{BI} + A^* R_B} \right)$$

$$P_{\perp} = \frac{P_{\parallel}}{1 + A^* R_B}$$

where r denotes the reference point (here the equatorial plane), R_B is the ratio between the magnitudes of the equatorial \mathbf{B} -field and the field at the location of interest, R_{BI} the ratio between the ionospheric field and that at the location of interest, while $A = P_{\parallel r}^*/P_{\perp r}^* - 1$, with $P_{\parallel r}^*$ and $P_{\perp r}^*$ related to the actual values at the reference point r through equation (9) of Liemohn [2003]. While this collisionless mapping does assume bi-Maxwellian distributions at the

reference point, the pressure results from the mapping have been shown to be very close to results from a kinetic model [Liemohn, 2003], rendering the method appropriate for our purpose, i.e., computing the force-balanced fields. In fact, the previous filled loss cone formalism is also fine for this purpose; while the empty loss cone assumption is more physically realistic (the pressure drops to zero at the ends of the field line, i.e., on the Earth's surface in the equilibrium model), the results obtained by employing it in the code are almost identical to those from the filled loss cone approach. This is because differences between the empty and the filled loss cone formalisms occur only close to the end of field lines [Liemohn, 2003], so the pressures in most of the domain (including all regions with high β_p) are about the same with the two mapping choices. We note that the final result of the code, a 3-D force-balanced configuration, also provides as a by-product a realistic mapping of the pressure profile in the whole computational domain.

3.2. Computational Domain

[29] The 3-D equilibrium model requires, besides pressure input, inner and outer magnetic flux (α) surfaces defining its computational domain, as well as the value of α on those surfaces. For this initial study we constructed those boundaries by field-line tracing using the T89 empirical field model [Tsyganenko, 1989], which is parameterized by the K_p index, known at each time during the storm. In Figure 1 we show the most “disturbed” computational domain, built with $K_p = 6$. The reason for using T89 was its speed and also its discrete K_p parameterization; since the T89 code provides only six discrete domains, we used linear interpolation to obtain the shape of the domain at any given time during the storm rather than explicitly tracing model field lines at each time. Future refinements of this study will include the use of the latest empirical magnetic field model of Tsyganenko and Sitnov [2005], which is parameterized by Dst and solar wind parameters, and which will explicitly provide a different computational domain at each time when an equilibrium configuration is to be computed. While realistic model boundaries are obviously important, we note however that in configurations with high plasma β_p the

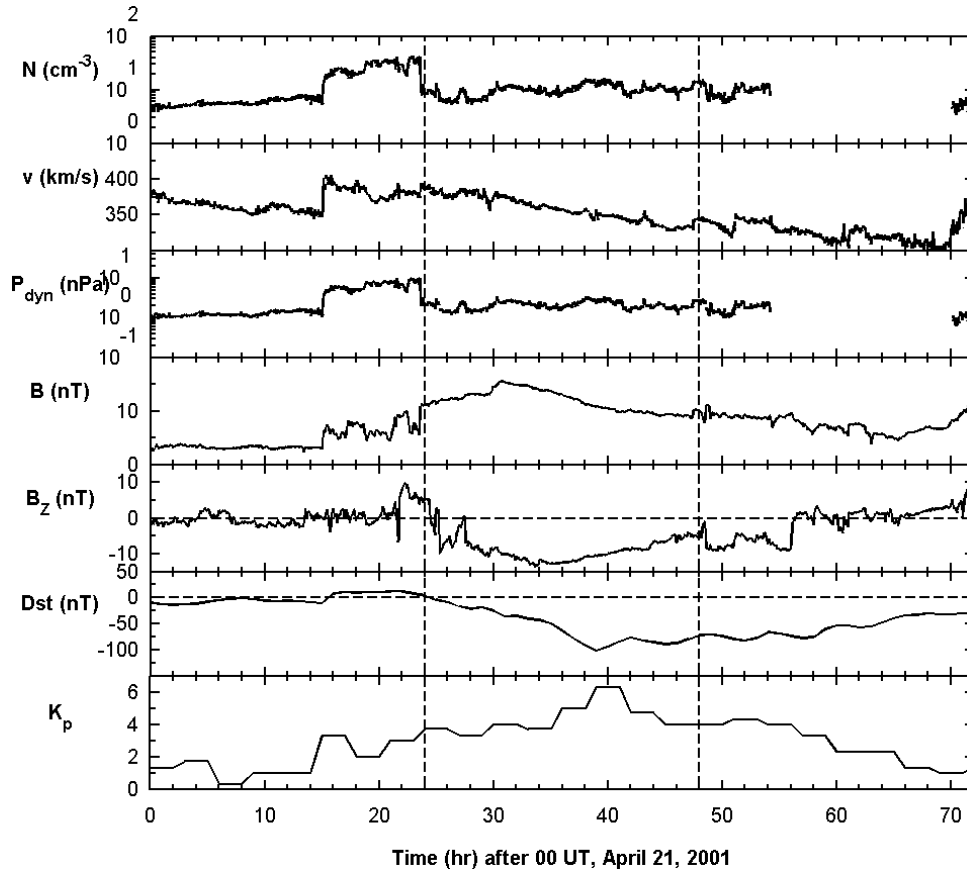


Figure 2. Solar wind parameters and Dst and K_p indices during the 22 April 2001 storm. The 24-hour interval simulated in this study is delimited by vertical dashed lines.

equilibrium solution not too close to the boundary does not depend too much on the boundary.

4. Self-Consistent Results

4.1. Field-Line Integrals in the Nondipolar Case

[30] Even before analyzing the actual results, we can anticipate that plasma transport will be quite different in the lower \mathbf{B} -fields of the self-consistent case compared to using a dipolar field. Indeed, we find that the h and I integrals (equations (8) and (9)) for the stretched field configurations found in the storm main phase are typically much lower on the nightside than the ones for a dipolar field, down by about 80% for the largest pitch angles (particles mirroring close to the equatorial plane). The large difference in a realistic versus dipolar field configuration means that the particle drifts will be strongly affected in the self-consistent framework.

4.2. Application to the 22 April 2001 Storm

[31] We apply our technique to the geomagnetic storm of 21–23 April 2001, a “challenge” event chosen for study by the NSF Geospace Environment Modeling (GEM) Program. This moderate storm (Dst minimum of -102 nT) was driven by a magnetic cloud with a southward field. The interplanetary shock was observed at ~ 1600 UT on 21 April and the storm main phase lasted more than 12 hours. The relevant solar wind parameters and the Dst and K_p indices are plotted in Figure 2.

[32] The computation presented here covers 24 hours of the storm, starting at 0000 UT on 22 April 2001 (at the beginning of the main phase, 8 hours after the interplanetary shock arrival) until 0000 UT on 23 April (early recovery phase). We present results at five representative hours during this interval. The Weimer 01 electric convection model [Weimer, 2001], an empirical model based on low-Earth-orbit satellite measurements, is used in RAM, as it usually gives more realistic values of the simulated Dst index [Jordanova *et al.*, 2006] than other convection models. The model depends on interplanetary conditions and predicts the strongest electric fields during the main phase of the storm. The RAM code was updated to take into account the particle drifts in the general magnetic field, but the loss terms in equation (7) were not changed for this study.

4.2.1. Plasma Pressure and Anisotropy

[33] In Figure 3 we show at the top the measured Dst index versus time. The Dst has a steady descent, reaching a minimum at around $T = 39$ hours. The middle and bottom plots show the perpendicular plasma pressure (P_{\perp}) in the equatorial plane at the five selected hours, for a run of the kinetic model with dipole magnetic field and for the self-consistent run, respectively (by the self-consistent run we mean the third iteration of the coupling procedure, as explained below). Both plots show the pressure increasing significantly during the storm main phase, with maxima reached in the dusk sector, consistent with the ion drifts. It is

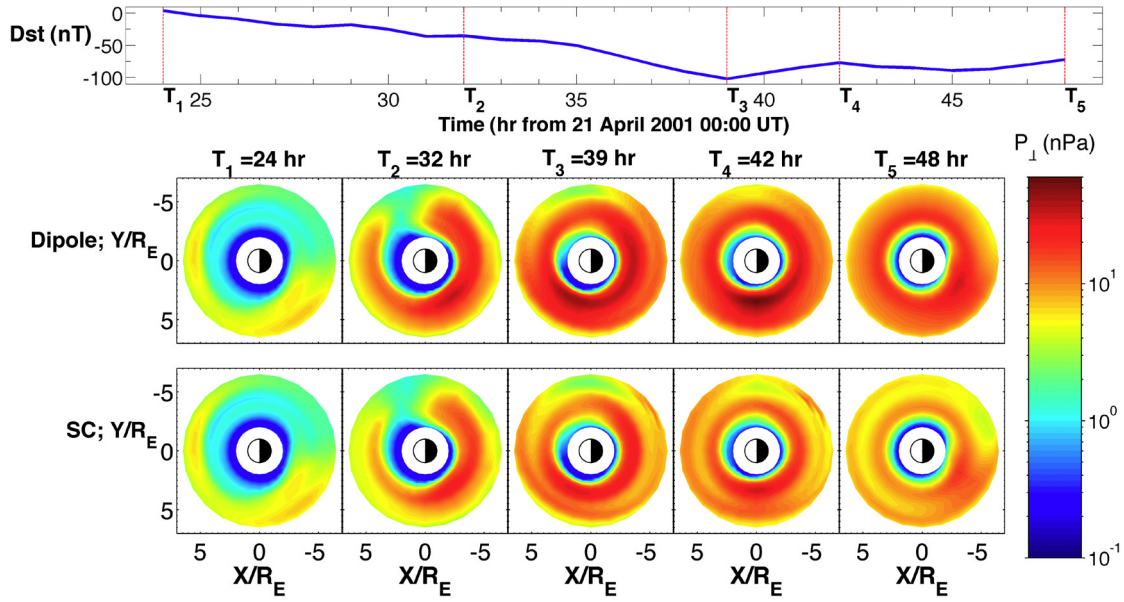


Figure 3. (top) Dst index during the April 2001 storm (time axis starts at 0000 UT on 21 April); (middle) pressure in the equatorial plane from RAM model run with dipole background; (bottom) pressure in the equatorial plane from the self-consistent simulation.

clear from the azimuthal asymmetry that increased convection plays a very important role in the ring current buildup. What is striking however is that in the self-consistent computation the maximum P_{\perp} reached is only half the value corresponding to the case when a dipole magnetic background is used, 30 nPa versus 60 nPa, respectively. As will be demonstrated in the Discussion section, this is mostly due to faster drifts leading to lower particle densities in the self-consistent case compared to runs with a dipole field.

[34] There are also other features that differentiate the self-consistent case from the dipole run, as seen in Figure 3.

Specifically, in the self-consistent case there are locally larger pressure values farther away from Earth, accompanied by local gradients and double peaks in the equatorial profile. Similar features, i.e., a decrease in P_{\perp} (versus runs with a dipole field) through most of the domain, accompanied by local increases farther from Earth, are also reported in the modeling study of *Chen et al.* [2006], who employ a simpler 2-D self-consistent formalism (in the equatorial plane). A different morphology in the self-consistent pressure results versus runs with inert fields is also found when taking into account changes in electric

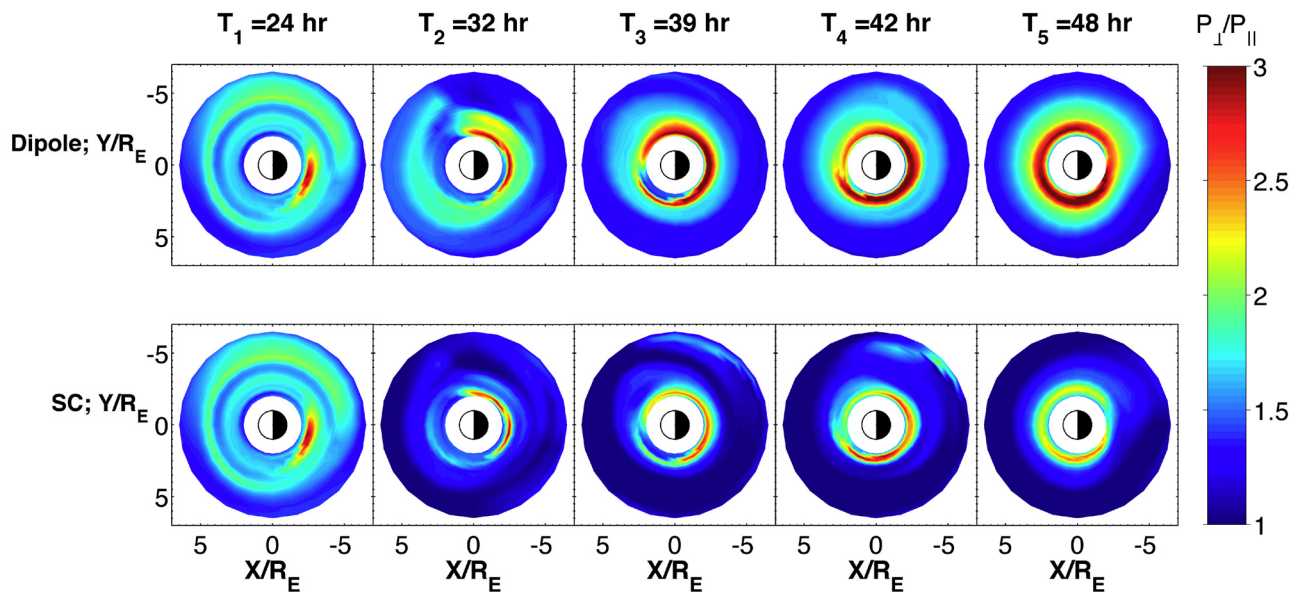


Figure 4. (top) P_{\perp}/P_{\parallel} in the equatorial plane from RAM model run with dipole background ($IT = 1$); (bottom) P_{\perp}/P_{\parallel} in the equatorial plane from the self-consistent simulation ($IT = 3$).

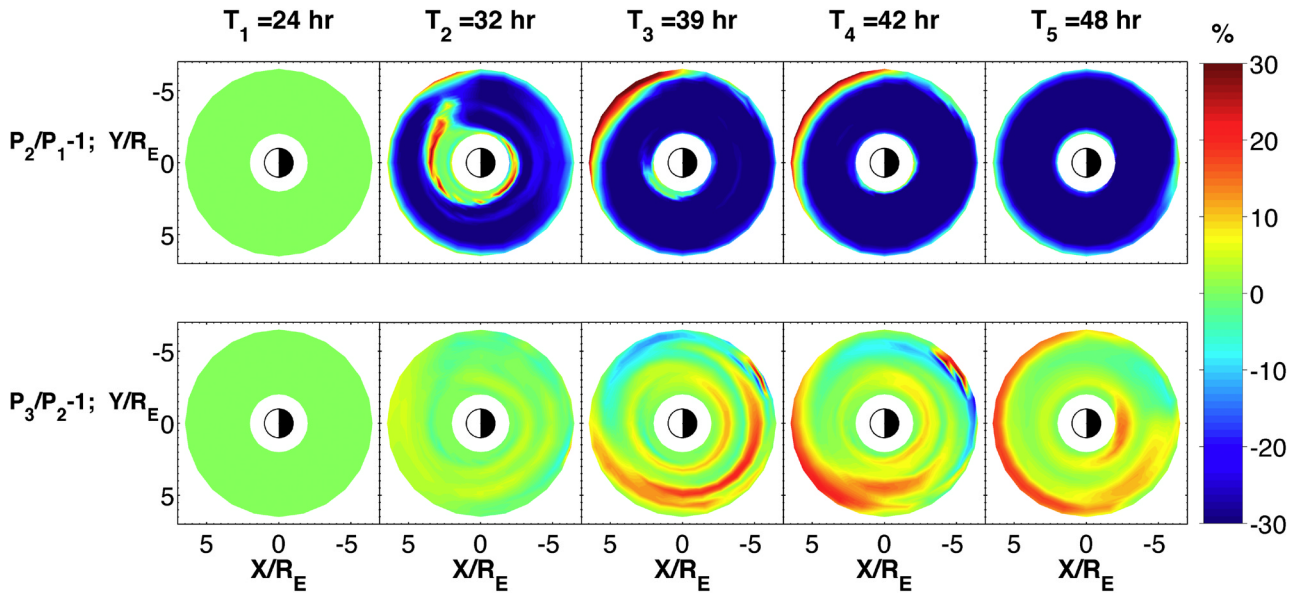


Figure 5. (top) Relative difference in the equatorial plane between pressures at the the second and the first iteration $(P_{\perp 2} - P_{\perp 1})/P_{\perp 1}$. The color plots are mostly saturated (indicating changes $>25\%$); (bottom) relative difference in the equatorial plane between pressures at the third and the second iteration $(P_{\perp 3} - P_{\perp 2})/P_{\perp 2}$.

rather than magnetic fields: considering the feedback of particles on the electric field leads to a picture with more discrete structure than from runs with unchanged fields [Liemohn *et al.*, 2004].

[35] Figure 4 shows the pressure anisotropy P_{\perp}/P_{\parallel} . It also exhibits significant differences between the dipole-background and the self-consistent case. Specifically, the anisotropy developed in the self-consistent case is lower than in the dipolar run. This feature is due to P_{\perp} being increased significantly less than in the dipolar run, while P_{\parallel} is increased almost as much as in the dipole field case. The physical cause for this is described in the Discussion section as well.

[36] The pressure anisotropy is significantly lower in the storm main phase compared to the early recovery phase, a feature also seen in observations [e.g., Sorbo *et al.*, 2005]. The lower anisotropy is also expected in the main phase from a plasma stability viewpoint: at that time the field is more stretched, plasma β_p is higher and therefore the instability thresholds are lower [e.g., Gary *et al.*, 1997]. The degree of anisotropy and its spatial structure are crucial quantities obtained as products of the self-consistent code coupling; their knowledge is important in studies of high-energy particles, as the anisotropy controls the growth of waves such as the electromagnetic ion cyclotron (EMIC) waves, which can strongly affect particles in the inner magnetosphere.

4.2.2. Convergence; Other Computed Quantities

[37] Convergence of the iterative coupling procedure is approached quite fast, after only three iterations. In Figure 5 we plot in the equatorial plane the relative difference between P_{\perp} at iterations 2 versus 1 and 3 versus 2, respectively. The figure shows that there is a large pressure change (mostly a decrease) from the first iteration (RAM

run with dipole field) to the second (first force-balanced field fed back into the RAM code), but only small changes from the second iteration to the third, thus allowing us to approximate the $IT = 3$ case to an ideally converged self-consistent computation.

[38] The next figure, Figure 6, shows in the top row the equatorial plane profiles of the difference between the self-consistent field and the Earth dipole field $B_{SC} - B_{dip}$; the bottom row shows the difference $B_{SC} - B_1$ between the self-consistent field and that obtained after the first iteration (i.e., force-balanced with plasma pressures from RAM with dipole field, similar to what we calculated before [Zaharia *et al.*, 2005]). One notices that the self-consistent magnetic field is significantly depressed from dipolar in the main phase of the storm. The largest depressions are at $T = 39$ hours, of less than -120 nT near midnight. The self-consistent field is also different from the field at $IT = 1$, but the differences are much lower in absolute magnitude than between it and the dipole field. The field at $IT = 1$ is in most places lower than B_{SC} by less than 20 nT, indicating that the first iteration “overshoots” the actual field stretching (as it does for the pressure, see Figure 5), but not by much. The self-consistent field is however significantly lower in very localized regions near the outer boundary, where it is more stretched in order to balance the plasma pressure peaks appearing there in the self-consistent case.

[39] Figure 7 shows in the equatorial plane the perpendicular plasma $\beta_{p\perp}$ in the self-consistent case, as well as the difference between it and $\beta_{p\perp}$ obtained at $IT = 1$. The self-consistent $\beta_{p\perp}$ has very large values during the storm main phase, reaching almost 50 in very localized regions in the equatorial plane at $T = 42$ hours. Notwithstanding those very localized peaks, $\beta_{p\perp}$ approaches values of 1 or larger for all distances $R > 4.5 R_E$ on the night side during the

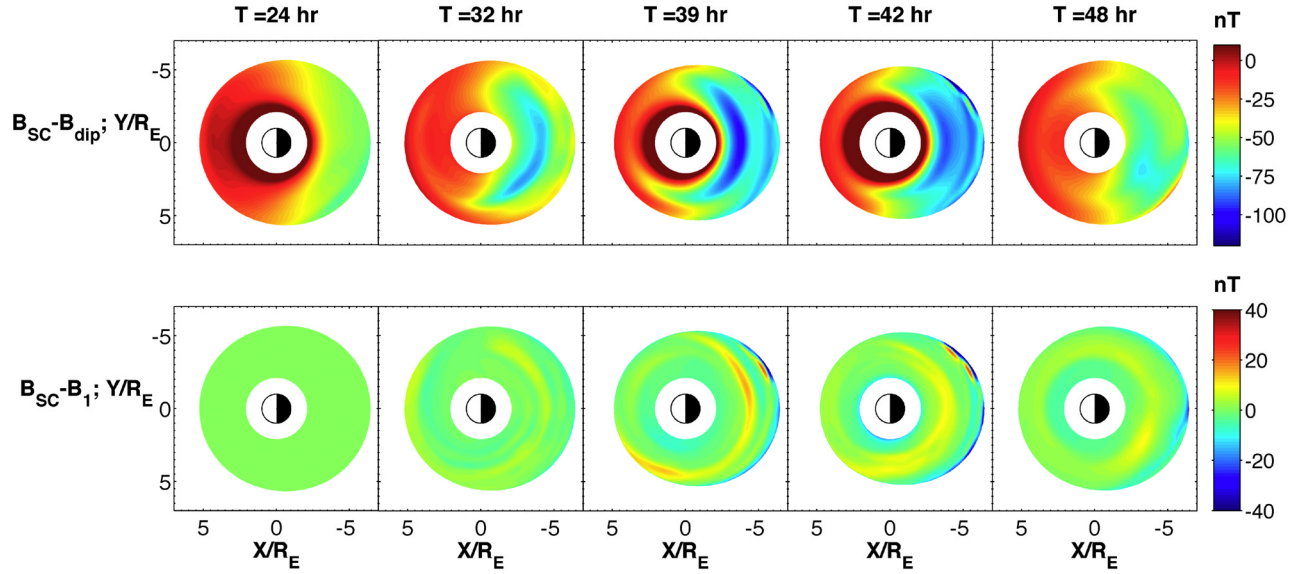


Figure 6. (top) Difference between the self-consistent magnetic field and the Earth dipole field, $B_{SC} - B_{dip}$, in the equatorial plane; (bottom) difference between the self-consistent field (i.e., obtained at $IT = 3$) and the force-balanced field at $IT = 1$.

storm main phase. This clearly shows why the magnetic field is so much changed from dipolar, as when plasma β_p is 1 or larger, the pressure becomes crucial in dictating the field configuration. The differences between the self-consistent values and those at $IT = 1$ again reflect the fact that the first iteration overshoots the amount of field stretching (leading to larger $\beta_{p\perp 1}$), except near the boundary, where the self-consistent $\beta_{p\perp}$ is larger due to the localized pressure peaks.

[40] The next figure, Figure 8, shows the azimuthal current density J_ϕ in the equatorial and the noon-midnight meridian planes, for both $IT = 1$ and the self-consistent case. As expected, the largest current densities ($|J_\phi| > 10$ nA/m²)

appear in the storm main phase (and to some extent in the early recovery phase) whenever the pressure is large. The maximum current density at those times is about an order of magnitude larger than before the storm. The large, asymmetric part of the current in the storm main phase is commonly referred to as the “partial ring current” [e.g., *Liemohn et al.*, 2001]. An interesting feature are the localized regions with large current density in the dawn sector in the self-consistent picture (seen at hours 39 and 42, these currents appear due to the localized peaks in plasma pressure at those times, as seen in Figure 3). The westward current at $IT = 3$ is slightly larger and more toward dusk than at $IT = 1$ at $T = 39$ hours and $T = 42$ hours, showing

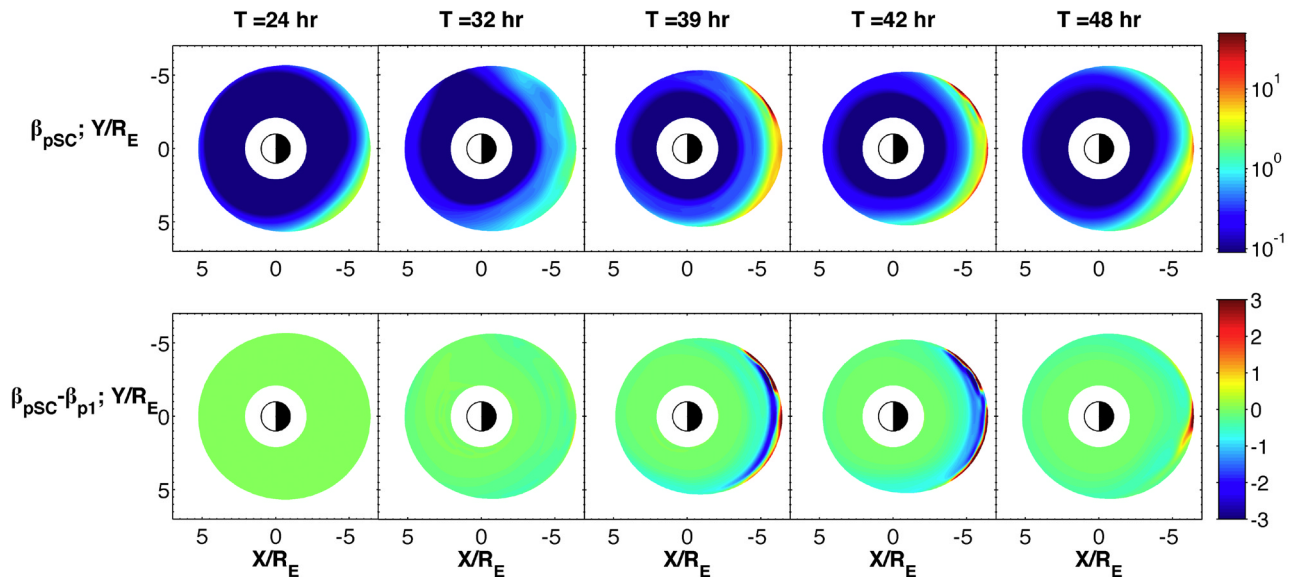


Figure 7. (top) Perpendicular plasma β_p in the equatorial plane in the self-consistent case ($IT = 3$); (bottom) difference between the self-consistent plasma β_p and that obtained at $IT = 1$.

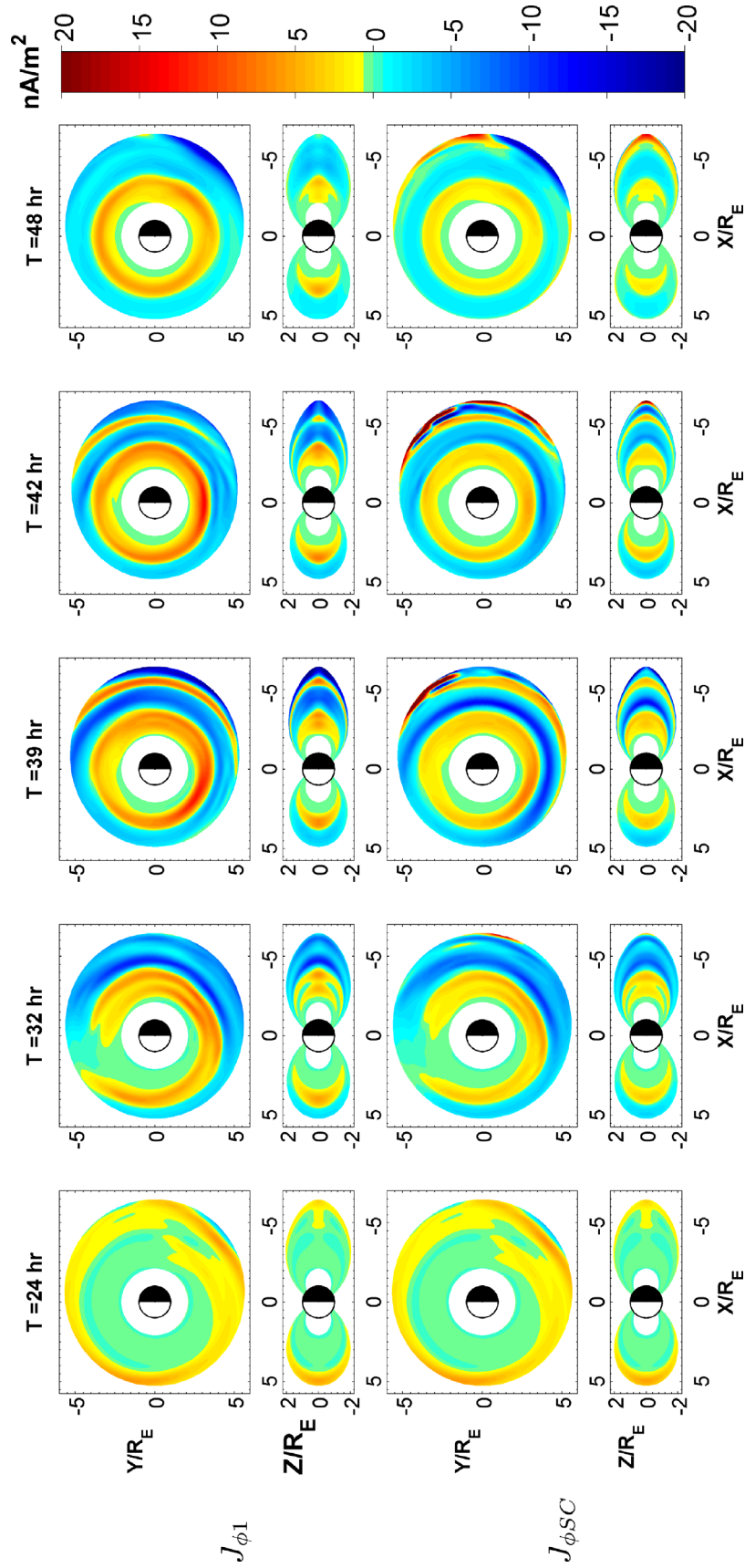


Figure 8. Top two rows show azimuthal current density J_ϕ (nA/m^2) in the equatorial and noon-midnight meridian planes, after the first iteration. Positive (negative) signs show currents that are eastward (westward) in the night side. Bottom two rows show the same quantities, but after the third iteration (self-consistent case).

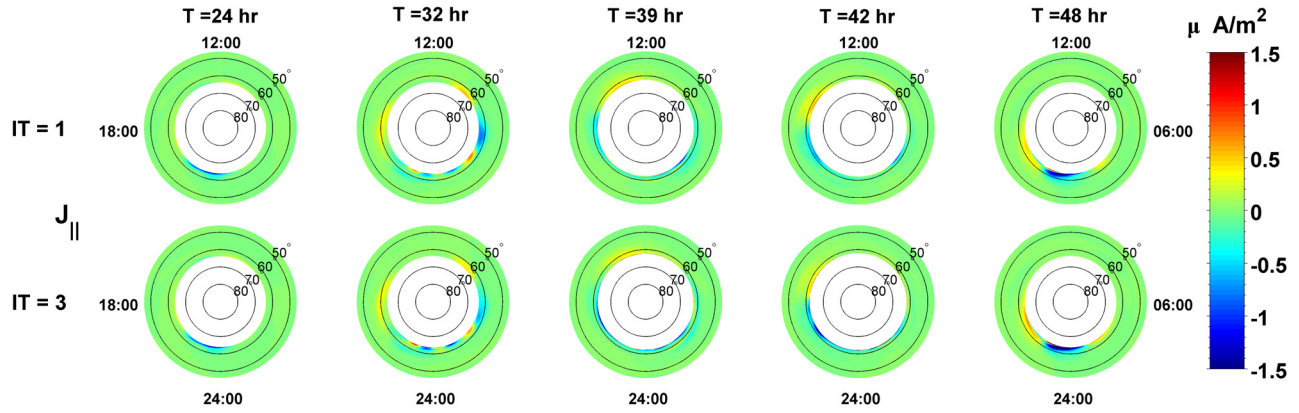


Figure 9. (top) Field-aligned (Birkeland) current density $J_{\parallel}(\mu\text{A}/\text{m}^2)$ at the top of the ionosphere, after $IT = 1$. Positive (negative) signs show currents into (out of) the ionosphere. The computational domain extends to lower ionospheric latitudes for higher Kps (hours 39, 42). (bottom) The same, but for $IT = 3$.

that while the pressures are lower in the self-consistent case compared to $IT = 1$, the earthward pressure gradients are slightly larger.

[41] In the noon-midnight meridian plots (for the $IT = 1$ case), we again notice that at the peak of storm activity, instead of being concentrated in the equatorial plane, the westward current far enough from Earth has a butterfly shape (see westward current close to the outer boundary in the $T = 42$ plot), with maxima above and below the plane, as also seen in our previous computations [Zaharia *et al.*, 2005, Figure 5]. Interestingly, this feature is not present anymore in the self-consistent picture because of the lower pressure anisotropy (the current bifurcation, as explained by Zaharia *et al.* [2005], only occurs in regions with both high β_p and high anisotropy).

[42] Other differences between the $IT = 1$ and the $IT = 3$ cases reflect those seen in the magnetic field depression and $\beta_{p\perp}$ plots: the current density J_{ϕ} is lower closer to Earth in the self-consistent case, but locally higher in the outer regions. We also notice the irregular current morphology farther from Earth: instead of a smooth westward current, the currents are widely distributed inside the 3-D domain; still, the westward-oriented currents dominate, and the total integrated current amounts to a net westward ring current that is the main cause of the Dst drop. At the peak of the storm main phase ($T = 39$) the integrated computed eastward azimuthal current is 0.42 MA (compared to 0.36 MA before the storm at $T = 24$). On the other hand, there is a large change in the integrated westward current: 1.7 MA at $T = 39$ vs. 0.31 MA at $T = 24$. While we likely capture all the eastward current in our domain, that is certainly not the case for the westward current. Indeed, additional currents are likely to flow outside our boundary (both at larger radii and also at larger Z values), therefore a comparison of total currents with observations is not straightforward. More relevant is comparing current densities, and we note that our obtained westward current densities compare well with statistical studies; e.g., Le *et al.* [2004] find typical current peaks of 11 nA/m² for storms with $-80 \text{ nT} > Dst > -100 \text{ nT}$ (which is slightly less intense than the present storm).

[43] Finally, we plot in Figure 9 the parallel (field-aligned) current density on the top of the ionosphere, obtained by Ampere's law from the 3-D \mathbf{B} -field. These

currents appear through the divergence of the perpendicular currents. They have an irregular structure and are rather large locally ($>1 \mu\text{A}/\text{m}^2$) during the main phase (these are significant values, keeping in mind that all the ionospheric latitudes considered here map to less than $6.6 R_E$ from Earth). The currents with large J_{\parallel} flow in very narrow sheets during the main phase, corresponding to the limited extent of the local peaks farther from Earth in the equatorial pressure and J_{ϕ} distribution; these narrow sheets become wider in the early recovery phase ($T = 48$ hours) when the peaks disappear. The currents are largest near the boundary, indicating that the boundary may have a significant effect on their values there. The exact dependence on the boundaries will be addressed in a future study. While clearly most of the field-aligned currents flow in regions beyond our modeling domain, we stress that the present calculation shows that significant J_{\parallel} can flow at lower latitudes; we also point out that the ability of our modeling technique to compute the self-consistent field-aligned currents is a very useful feature for the future addition of convective field self-consistency by coupling the present approach with an ionospheric model through the field-aligned currents.

5. Discussion

[44] Our approach is unique in that the computed \mathbf{B} -fields are force-balanced in full 3-D with anisotropic pressures from a kinetic model; other methods of computing force-balanced fields either use isotropic pressure as the magneto-frictional method [Hesse and Birn, 1993; Toffoletto *et al.*, 1996, 2001; Lemon *et al.*, 2004] or are less than three-dimensional [Chen *et al.*, 2006].

[45] In this section we explore in more detail the reason for the main results of this study, i.e., the significant perpendicular plasma pressure decrease obtained when self-consistency is taken into account compared to using a dipolar field in the RAM model. The lower pressure can be because of lower temperature (i.e., energization efficiency) or lower particle density. Looking at Figure 10, which shows the total ion density n at $IT = 1$ and $IT = 3$, it is clear that the latter reason (i.e., lower densities) is the cause for the lower P_{\perp} . This is not unexpected; with the same

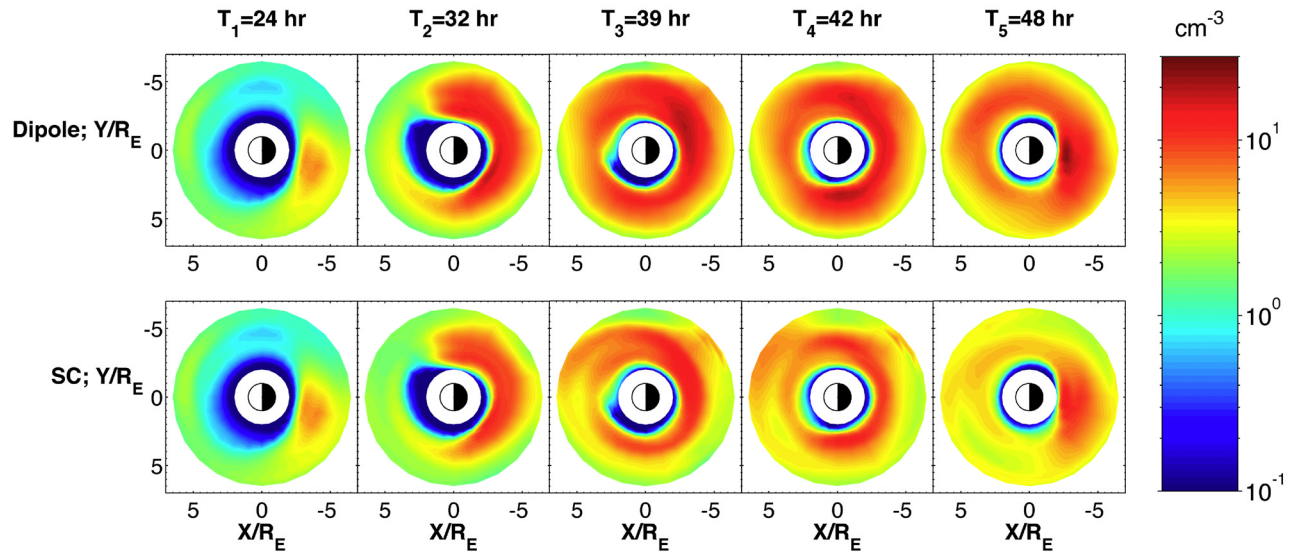


Figure 10. (top) Total ion density (H^+ , He^+ , and O^+) in the equatorial plane from RAM model run with dipole background ($IT = 1$); (bottom) ion density in the equatorial plane at $IT = 3$ (self-consistent).

geosynchronous boundary conditions, the particle drifts in the present case are significantly faster (due to the lower magnetic field) than in the case with a dipolar background. Since the same particle flux is injected from the geosynchronous orbit, flux conservation leads to lower densities and thus lower pressures.

[46] Now that we showed that the P_{\perp} decrease is due to lower densities, the remaining question is why P_{\parallel} does not experience a similar decrease (P_{\parallel} is not much changed, as can be seen from the P_{\perp} and P_{\perp}/P_{\parallel} plots). Obviously there must be a discrepancy in how the energization of small and large pitch angles, respectively, is affected in the self-consistent magnetic field compared to a dipole. Particles that make up the perpendicular pressure are mostly those with large pitch angles. They are energized mainly through betatron acceleration, depending on the ratio of the field values at the final versus initial position. During the storm main phase, the field is lower both at geosynchronous and inside the domain at the final particle location, so it is not clear how this ratio should be affected. Analyzing P_{\perp}/n (not shown here) we find that it is not affected much, i.e., the efficiency of betatron acceleration is about the same for particles starting at $6.6 R_E$, whether they move in a dipole field or a self-consistent field. On the other hand, particles which make up the parallel pressure are mostly those with small pitch angles, and they are accelerated mostly by Fermi acceleration, as the length of the field lines they bounce along decreases with approaching Earth. Relevant to those particles, we find P_{\parallel}/n to be larger in the self-consistent (SC) case compared to the dipolar run; this indicates that the Fermi acceleration mechanism is more effective in the SC case compared to the dipole case, i.e., there is a larger change in the field line length along the drift trajectory in the SC case compared to that in the run with a dipole field. Two factors contribute to this: both the different field configuration itself, and the change in the drift trajectories in the self-consistent framework. We find that in a more stretched field geometry the share of the Fermi mechanism

in the total energization becomes larger, a result found at larger distances by [Sergeev *et al.*, 2001].

[47] Thus the significant decrease in P_{\perp} and P_{\perp}/P_{\parallel} at the same time in the SC case is due to changes in both density and energization: as drift velocities are increased, the particle density decreases; on the new drift trajectories and in the more stretched field, particles with small pitch angles are energized more than in a dipole field, while those with large pitch angles do not experience much change in energization compared to the dipole case.

[48] We want to stress however that the results presented here are just initial results, obtained by an iterative coupling at one-hour intervals of the two models. Furthermore, for this study only the particle drifts (the left-hand side) in equation (7) have been updated so far in the RAM code for the nondipole field. The bounce-averaging of losses (the right-hand side of the equation) has not. The update of the loss terms could change some result details: for example, the pressure anisotropy depends on charge-exchange (the strongest loss mechanism), and a change in this could affect the parallel versus perpendicular pressures disproportionately (e.g., particles that go closer to Earth experience a higher neutral density and thus more charge-exchange collisions). It is likely however that the main result of the study, the less efficient increase in particle density and perpendicular pressures, will be maintained in a completely updated formalism, owing to it being due to significantly changed particle drifts in the nondipolar field.

[49] We discuss now the appearance of local peaks in the pressure profile in the SC case, mostly near the outer boundary. This is also due to the self-consistent magnetic field strongly changing the particle drifts. In such a case, unlike in a dipole field, locally closed drift paths can develop [e.g., Ebihara and Ejiri, 2000], which will maintain a local pressure peak for a while. The actual local structure that develops is due to the interplay between changes in the boundary particle distributions that are injected into the domain and such strong modifications of the drift trajectory

ries in the self-consistent field. The pressure peaks that appear correspond to sharp gradients, and for some hours in the storm main phase the equilibrium computation had to be performed with a larger number of grid points in order to be numerically stable.

[50] Our field calculation method, which uses Dirichlet boundary conditions on fixed boundaries, does have a limitation, in that it assumes a given total magnetic flux inside the domain. Therefore, the model used to obtain the boundaries has to be realistic. In particular, the solution very close to the boundary will be forced to resemble the empirical field; however, even on the boundary the field lines are allowed to slide in the azimuthal direction. Moreover, farther away the solution does not depend too much on the boundary, because of the large β_p (thus the nonlinear right-hand side terms in equations (3) and (4) are more important in determining the solution).

[51] As mentioned, another limitation of this initial study is that we calculated the self-consistent solution exchanging pressure and field information between the two codes at every hour only. This time interval is certainly less than ideal but was dictated by practical considerations of computational time. The current work is therefore just a first step toward a better solution: the final results may be modified when full coupling between the two codes is achieved by updating the solution at a smaller time step. We are currently working on the parallelization of the constituent codes, which will allow a 5-min coupling between them on a routine basis. Results from such a coupling (which will include using the latest empirical magnetic field model of *Tsyganenko and Sitnov* [2005] to compute a different domain at each 5-min interval) will be presented in future extensions of this work.

[52] Finally, we note that the results also depend on the choice of the electric field used in the RAM model. In this study we use the large-scale Weimer 01 empirical convection field model [Weimer, 2001]; thus we do not consider local features such as the narrow regions of intensified \mathbf{E} -fields known as SAPS [Foster and Burke, 2002]. Furthermore, the inductive electric fields due to nonzero $\partial\mathbf{B}/\partial t$ are not yet included in the coupled model. Their inclusion, however, will be greatly facilitated by the Euler potential representation of the \mathbf{B} -field in the equilibrium code and will be considered in the future, along with a more realistic convection electric field.

6. Summary and Conclusions

[53] Kinetic models are crucial tools in the study of the inner magnetosphere and of geomagnetic storms in particular. The RAM code [Jordanova et al., 2006] reproduces many features of the inner magnetosphere during storms; however, it has used a dipole background magnetic field so far, which is not consistent with the plasma distribution. In this paper we present an important improvement to RAM: following the previous 1-way coupling [Zaharia et al., 2005], we develop an initial iterative 2-way (self-consistent) coupling between a 3-D plasma equilibrium code and the RAM model. This is done by updating the bounce-averaged particle drift formalism to arbitrary \mathbf{B} in RAM, computing the magnetic field in force balance with anisotropic pressures from RAM, and then feeding that field back into the

kinetic model to drive its continued evolution. We apply this method to the particular case of the 22 April 2001 storm, employing an iterative procedure until convergence (which is approached quickly, after only three iterations).

[54] The computed storm-time physical quantities are found to be significantly different from those obtained by using a dipolar magnetic field in RAM. In particular, plasma quantities are significantly modified, with lower particle density, perpendicular plasma pressure and anisotropy found inside geosynchronous orbit. The self-consistently computed magnetic field is found to be depressed from dipolar, with decreases of more than 120 nT in absolute magnitude at 5 R_E on the nightside. The very changed field modifies: (1) the particle drift trajectories (with faster drifts leading to lower particle densities) and (2) the particle energization (the Fermi mechanism becomes more effective than in a dipole field, while the betatron acceleration effectiveness does not change much), which leads to decreases in P_\perp and P_\perp/P_\parallel .

[55] Another interesting feature of the self-consistent simulation is the appearance of local, narrow pressure (and density) peaks in certain locations, unlike the very smooth picture obtained with a non self-consistent magnetic field. Also, plasma β_p is locally higher on the nightside in the self-consistent case, with important repercussions for plasma stability there.

[56] Finally, another important result of the study is the finding that plasma β_p in the inner magnetosphere at the peak of storm activity can be significant, i.e., larger than 1. This shows that plasma pressure is crucial in influencing the magnetic field configuration and reinforces our previous conclusion [Zaharia et al., 2005] that a magnetically self-consistent approach is needed for inner magnetosphere modeling during storms. In other words, during a geomagnetic storm the plasma energy density becomes comparable to or larger than the field energy density, leading to large changes in the field configuration, whose effects need to be considered in a self-consistent manner. This work provides such an approach, and is currently the only one in full three dimensions with the inclusion of nonisotropic pitch angle distributions.

[57] **Acknowledgments.** We thank the reviewers for their suggestions, which have improved the manuscript. This work was performed under the auspices of the U.S. Department of Energy, with support from the DoE NA-22 and the Los Alamos LDRD DREAM programs. Additional support is acknowledged from NASA's Living With a Star TR&T program.

[58] Amitava Bhattacharjee thanks the reviewers for their assistance in evaluating this paper.

References

- Barber, C. B., D. P. Dobkin, and H. T. Huhdanpaa (1996), The Quickhull algorithm for convex hulls, *Trans. Math. Software*, 22(4), 469.
- Belian, R. D., G. R. Gisler, T. Cayton, and R. Christensen (1992), High-Z energetic particles at geosynchronous orbit during the great solar proton event series of October 1989, *J. Geophys. Res.*, 97(A11), 16,897.
- Cahill, L. J., Jr. (1973), Magnetic storm inflation in the evening sector (Magnetic storm inflation analysis from Explorer 45 and ground observation data, noting proton penetration into magnetosphere evening quadrant), *J. Geophys. Res.*, 78, 4724.
- Chen, M. W., L. R. Lyons, and M. Schulz (1994), Simulations of phase space distributions of storm time proton ring current, *J. Geophys. Res.*, 99(A4), 5745.
- Chen, M. W., S. Liu, M. Schulz, J. L. Roeder, and L. R. Lyons (2006), Magnetically self-consistent ring current simulations during the 19 October 1998 storm, *J. Geophys. Res.*, doi:10.1029/2006JA011620, in press.

- Chen, Y., R. H. W. Friedel, G. D. Reeves, T. G. Onsager, and M. F. Thomsen (2005), Multisatellite determination of the relativistic electron phase space density at geosynchronous orbit: Methodology and initial results during geomagnetically quiet times, *J. Geophys. Res.*, **110**, A10210, doi:10.1029/2004JA010895.
- Cheng, C. Z. (1995), Three-dimensional magnetospheric equilibrium with isotropic pressure, *Geophys. Res. Lett.*, **22**, 2401.
- De Zeeuw, D. L., S. Sazykin, R. A. Wolf, T. I. Gombosi, A. J. Ridley, and G. Tóth (2004), Coupling of a global MHD code and an inner magnetospheric model: Initial results, *J. Geophys. Res.*, **109**, A12219, doi:10.1029/2003JA010366.
- Ebihara, Y., and M. Ejiri (2000), Simulation study on fundamental properties of the storm-time ring current, *J. Geophys. Res.*, **105**, 15,843.
- Ebihara, Y., M.-C. Fok, R. A. Wolf, T. J. Immel, and T. E. Moore (2004), Influence of ionosphere conductivity on the ring current, *J. Geophys. Res.*, **109**, A08205, doi:10.1029/2003JA010351.
- Ejiri, M. (1978), Trajectory traces of charged particles in the magnetosphere, *J. Geophys. Res.*, **83**, 4798.
- Fok, M.-C., and T. E. Moore (1997), Ring current modeling in a realistic magnetic field configuration, *Geophys. Res. Lett.*, **24**(14), 1775.
- Foster, J. B., and W. J. Burke (2002), SAPS: A new characterization for sub-auroral electric fields, *Eos Trans. AGU*, **83**(36), 393.
- Ganushkina, N. Y., T. I. Pulkkinen, M. V. Kubyshkina, H. J. Singer, and C. T. Russell (2002), Modeling the ring current magnetic field during storms, *J. Geophys. Res.*, **107**(A7), 1092, doi:10.1029/2001JA900101.
- Gary, S. P., J. Wang, D. Winske, and S. A. Fuselier (1997), Proton temperature anisotropy upper bound, *J. Geophys. Res.*, **102**(A12), 27,159.
- Harel, M., R. A. Wolf, P. H. Reiff, W. Spiro, W. J. Burke, F. J. Rich, and M. Smiddy (1981), Quantitative simulation of a magnetospheric substorm: 1. Model logic and overview, *J. Geophys. Res.*, **86**, 2217.
- Hesse, M., and J. Birn (1993), Three-dimensional magnetotail equilibria by numerical relaxation techniques, *J. Geophys. Res.*, **98**, 3973.
- Jordanova, V. K., and Y. Miyoshi (2005), Relativistic model of ring current and radiation belt ions and electrons: Initial results, *Geophys. Res. Lett.*, **32**, L14104, doi:10.1029/2005GL023020.
- Jordanova, V. K., J. U. Kozyra, G. V. Khazanov, A. F. Nagy, C. E. Rasmussen, and M.-C. Fok (1994), A bounce-averaged kinetic model of the ring current ion population, *Geophys. Res. Lett.*, **21**(25), 2785.
- Jordanova, V. K., J. U. Kozyra, A. F. Nagy, and G. V. Khazanov (1997), Kinetic model of the ring current-atmosphere interactions, *J. Geophys. Res.*, **102**(A7), 14,279.
- Jordanova, V. K., C. J. Farrugia, R. M. Thorne, G. V. Khazanov, G. D. Reeves, and M. F. Thomsen (2001), Modeling ring current proton precipitation by electromagnetic ion cyclotron waves during the May 14–16, 1997, storm, *J. Geophys. Res.*, **106**(A1), 7.
- Jordanova, V. K., Y. Miyoshi, S. Zaharia, M. F. Thomsen, G. D. Reeves, D. Evans, C. Mouikis, and J. Fennell (2006), Kinetic simulations of ring current evolution during the Geospace Environment Modeling Challenge events, *J. Geophys. Res.*, doi:10.1029/2006JA011644, in press.
- Khazanov, G. V., M. W. Liemohn, T. S. Newman, M.-C. Fok, and R. W. Spiro (2003), Self-consistent magnetosphere-ionosphere coupling: Theoretical studies, *J. Geophys. Res.*, **108**(A3), 1122, doi:10.1029/2002JA009624.
- Le, G., C. T. Russell, and K. Takahashi (2004), Morphology of the ring current derived from magnetic field observations, *Ann. Geophys.*, **22**, 1267.
- Lemon, C., R. A. Wolf, T. W. Hill, S. Sazykin, R. W. Spiro, F. R. Toffoletto, J. Birn, and M. Hesse (2004), Magnetic storm ring current injection modeled with the Rice Convection Model and a self-consistent magnetic field, *Geophys. Res. Lett.*, **31**, L21801, doi:10.1029/2004GL020914.
- Liemohn, M. W. (2003), Yet another caveat to using the Dessler-Parker-Sckopke relation, *J. Geophys. Res.*, **108**(A6), 1251, doi:10.1029/2003JA009839.
- Liemohn, M. W., J. U. Kozyra, M. F. Thomsen, J. L. Roeder, G. Lu, J. E. Borovsky, and T. E. Cayton (2001), The dominant role of the asymmetric ring current in producing the storm-time *Dst*, *J. Geophys. Res.*, **106**, 10,883.
- Liemohn, M. W., A. J. Ridley, J. U. Kozyra, D. L. Gallagher, and D. M. Ober (2004), Analysis of conductance effects on inner magnetospheric electric fields, paper presented at Yosemite Workshop on Inner Magnetosphere Interactions, Southwest Res. Inst., Yosemite, Calif.
- Liemohn, M. W., A. J. Ridley, P. C. Brandt, D. L. Gallagher, J. U. Kozyra, D. M. Ober, D. G. Mitchell, E. C. Roelof, and R. DeMajistre (2005), Parametric analysis of nightside conductance effects on inner magnetospheric dynamics for the 17 April 2002 storm, *J. Geophys. Res.*, **110**, A12S22, doi:10.1029/2005JA011109.
- McComas, D. J., S. J. Bame, B. L. Barraclough, J. R. Donart, R. C. Elphic, J. T. Gosling, M. B. Moldwin, K. R. Moore, and M. F. Thomsen (1993), Magnetospheric plasma analyzer (MPA): Initial three-spacecraft observations from geosynchronous orbit, *J. Geophys. Res.*, **98**, 13,453.
- Piessens, R., E. deDoncker-Kapenga, C. Überhuber, and D. Kahaner (1983), *Quadpack: A Subroutine Package for Automatic Integration*, Springer, New York.
- Raeder, J., R. Walker, and M. Ashour-Abdalla (1995), The structure of the distant geomagnetic tail during long periods of northward IMF, *Geophys. Res. Lett.*, **22**, 349.
- Ridley, A. J., and M. W. Liemohn (2002), A model-derived storm time asymmetric ring current driven electric field description, *J. Geophys. Res.*, **107**(A8), 1151, doi:10.1029/2001JA000051.
- Roederer, J. G. (1967), On the adiabatic motion of energetic particles in a model magnetosphere, *J. Geophys. Res.*, **72**, 981.
- Roederer, J. G. (1970), *Dynamics of Geomagnetically Trapped Radiation*, 87 pp., Springer, New York.
- Sazykin, S., R. A. Wolf, R. W. Spiro, T. I. Gombosi, D. L. D. Zeeuw, and M. F. Thomsen (2002), Interchange instability in the inner magnetosphere associated with geosynchronous particle flux decreases, *Geophys. Res. Lett.*, **29**(10), 1448, doi:10.1029/2001GL014416.
- Sergeev, V. A., W. Baumjohann, and K. Shiokawa (2001), Bi-directional electron distributions associated with near-tail electron transport, *Geophys. Res. Lett.*, **28**(19), 3813.
- Sorbo, M., F. Soraas, K. Aarsnes, K. Oksavik, and D. S. Evans (2005), Low latitude precipitation of energetic neutral atoms reflects the ring current pitch angle distribution during storms, *Eos Trans. AGU*, **86**(52), Fall Meet. Suppl., Abstract SM41C-1206.
- Toffoletto, F. R., R. W. Spiro, R. A. Wolf, M. Hesse, and J. Birn (1996), Self-consistent modeling of inner magnetospheric convection, in *Third International Conference on Substorms (ICS-3)*, edited by E. J. Rolfe and B. Kaldeich, p. 223, Eur. Space Agency, Noordwijk, Netherlands.
- Toffoletto, F. R., J. Birn, M. Hesse, R. W. Spiro, and R. A. Wolf (2001), Modeling inner magnetospheric electrodynamics, in *Space Weather, Geophys. Monogr. Ser.*, vol. 125, edited by P. Song, G. L. Siscoe, and H. J. Singer, p. 313, AGU, Washington, D. C.
- Toffoletto, F. R., S. Sazykin, R. Spiro, R. Wolf, and J. Lyon (2004), RCM meets LFM: Initial results of one-way coupling, *J. Atmos. Sol. Terr. Phys.*, **66**, 1361.
- Tsyganenko, N. A. (1989), A magnetospheric field model with a warped tail current sheet, *Planet. Space Sci.*, **37**, 5.
- Tsyganenko, N. A., and M. I. Sitnov (2005), Modeling the dynamics of the inner magnetosphere during strong geomagnetic storms, *J. Geophys. Res.*, **110**, A03208, doi:10.1029/2004JA010798.
- Tsyganenko, N. A., and D. P. Stern (1996), Modeling the global magnetic field of the large-scale Birkeland current systems, *J. Geophys. Res.*, **101**, 27,187.
- Tsyganenko, N. A., H. J. Singer, and J. C. Kasper (2003), Storm-time distortion of the inner magnetosphere: How severe can it get?, *J. Geophys. Res.*, **108**(A5), 1209, doi:10.1029/2002JA009808.
- Weimer, D. R. (2001), An improved model of ionospheric electric potentials including substorm perturbations and application to the geospace environment modeling November 24, 1996, event, *J. Geophys. Res.*, **106**(A1), 407.
- Wolf, R. A. (1983), The quasi-static (slow-flow) region of the magnetosphere, in *Solar-Terrestrial Physics: Principles and Theoretical Foundations*, edited by R. L. Carovillano and J. M. Forbes, p. 303, Springer, New York.
- Zaharia, S. (2003), 3-D Magnetospheric structures and energetic particle injections, Ph.D. thesis, Princeton Univ., Princeton, N. J.
- Zaharia, S., and C. Z. Cheng (2003a), Near-Earth thin current sheets and Birkeland currents during substorm growth phase, *Geophys. Res. Lett.*, **30**(17), 1883, doi:10.1029/2003GL017456.
- Zaharia, S., and C. Z. Cheng (2003b), Can an isotropic plasma pressure distribution be in force balance with the T96 model field?, *J. Geophys. Res.*, **108**(A11), 1412, doi:10.1029/2002JA009501.
- Zaharia, S., C. Z. Cheng, and K. Maczawa (2004), 3-D Force-balanced magnetospheric configurations, *Ann. Geophys.*, **22**, 251, doi:10.1432-0576/ag/2004-22-251.
- Zaharia, S., V. K. Jordanova, M. F. Thomsen, J. Birn, M. H. Denton, and C. Z. Cheng (2005), Effect of storm-time plasma pressure on the magnetic field in the inner magnetosphere, *Geophys. Res. Lett.*, **32**, L03102, doi:10.1029/2004GL021491.

V. K. Jordanova, Space Science Center, University of New Hampshire, 410 Morse Hall, 39 College Road, Durham, NH 03824, USA.

G. D. Reeves, M. F. Thomsen, and S. Zaharia, Space Science and Applications (ISR-1), Los Alamos National Laboratory, P.O. Box 1663, MS D466, Los Alamos, NM 87545, USA. (szaharia@lanl.gov)